Small

NANO · MICRO small
www.small-journal.com

RESEARCH ARTICLE

In Situ Single-Particle LSPR Biosensor for Amplification-Free Detection of miR-451 via Dark-Field Scattering Spectroscopy

Xingyu Zi[1,2] | Hongen Cheng[1,2] | Jianqi Wang[1,2] | Kuilin Liu[1,2] | Xinyu Gao[4] | Guohua Liu[1,2,3] | Mingqing Zhang[4]

[1]College of Electronic Information and Optical Engineering, Nankai University, Tianjin, China | [2]Tianjin Key Laboratory of Optoelectronic Sensor and Sensing Network Technology, Tianjin, China | [3]Engineering Research Center of Thin Film Optoelectronics Technology, Ministry of Education, Nankai University, Tianjin, China | [4]Department of Colorectal Surgery, Tianjin Union Medical Center, The First Affiliated Hospital of Nankai University, Tianjin, China

Correspondence: Guohua Liu (liugh@nankai.edu.cn) | Mingqing Zhang (zmq@nankai.edu.cn)

Received: 13 August 2025 | **Revised:** 25 April 2026 | **Accepted:** 14 May 2026

Keywords: AuNPs | in situ detection | localized surface plasmon resonance | miR-451

ABSTRACT

Colorectal cancer (CRC) is frequently diagnosed at advanced stages due to the asymptomatic nature of early disease and the semi-invasive nature of colonoscopy. Developing effective noninvasive methods for CRC-related biomarker detection is crucial for reducing CRC mortality. Notably, miR-451 has been reported as a CRC-related biomarker candidate. We present an in situ single-particle spectroscopic assay for amplification-free quantitative detection of miR-451 using gold nanoparticles (AuNPs). Functionalized substrates with immobilized AuNPs enable real-time monitoring of localized surface plasmon resonance (LSPR) peak shifts at the single-particle level. By statistically analyzing the proportion of AuNPs exhibiting LSPR shifts, we achieved quantitative detection of miR-451. This in situ microfluidic configuration allows spectral analysis of the same nanoparticles before and after detection, eliminating spatial sampling errors. Specificity is conferred by a stem-loop DNA probe on the AuNP surface via strand displacement. The main advance lies in in situ tracking of the same immobilized nanoparticles with statistical single-particle readout. This strategy demonstrates a detection limit of 58 fM and excellent specificity against other miRNAs, with proof-of-concept feasibility in spiked FBS samples.

1 | Introduction

Colorectal cancer (CRC) is one of the leading causes of mortality [1, 2]. Currently, early screening for colorectal cancer is considered one of the most effective methods to reduce mortality and improve survival rates [3]. However, most colorectal cancer patients are diagnosed at advanced stages, primarily because early and intermediate stages lack obvious clinical symptoms, and colonoscopy, the gold standard for colorectal cancer detection, is an invasive procedure often resisted by patients [4]. Hence, there is an urgent need to develop non-invasive methods for the detection of CRC-related biomarkers. Prior research has shown that the expression levels of microRNA(miRNA) in human blood and feces are significantly associated with the prevalence of colorectal cancer. Among them, miR-451 has been proven to be widely dysregulated in human malignancies and plays a critical role in tumorigenesis and progression [5], thus, miR-451 is a promising biomarker candidate for colorectal cancer-related studies.

Significant effort has been devoted to developing methods for miRNA detection [6], Traditional miRNA detection techniques include northern blotting [7–9], microarray analysis [10, 11], and quantitative polymerase chain reaction (qPCR) [12, 13]. Among these techniques, northern blotting has been extensively applied in miRNA detection but is limited by low throughput,

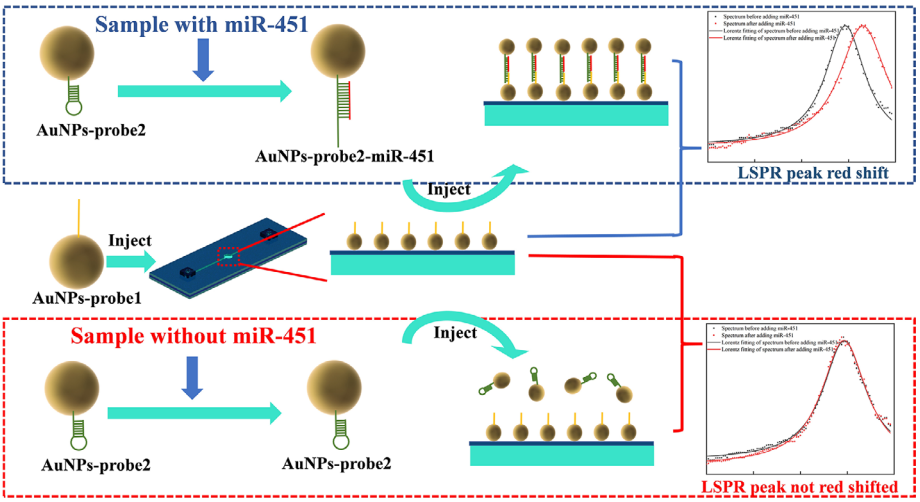

SCHEME 1 | Scheme of the in situ detection strategy for miR-451 based on LSPR.

cumbersome procedures, and inadequate sensitivity. Microarray analysis is advantageous for its high throughput and speed, however, it suffers from high costs and limited sensitivity [10, 11, 14, 15]. Reverse transcription quantitative polymerase chain reaction (RT-qPCR), a component of qPCR technology, is recognized as the gold standard for miRNA detection owing to its extensive dynamic range, exceptional sensitivity, and high sequence specificity. Nevertheless, difficulties in primer design, elevated false-positive rates, and the interconnected nature of its steps make reproducible and precise quantification particularly challenging [16].

Fluorescence imaging, surface-enhanced Raman spectroscopy (SERS), electrochemical methods, electrochemiluminescence (ECL), and localized surface plasmon resonance (LSPR) are among the prominent techniques for novel miRNA detection. Fluorescence imaging offers advantages including real-time capability, in situ analysis, and low cost [17, 18]. However, its detection sensitivity is hampered by photobleaching, background autofluorescence, and susceptibility to environmental changes. SERS possesses high sensitivity and selectivity, yet its application is limited by inherently weak SERS signals and potential interference from fluorescent backgrounds [19, 20]. Furthermore, the requirement for uniform SERS substrates and the challenges associated with their reusability significantly elevate the cost of SERS-based assays. Electrochemical methods exhibit high specificity [21, 22], but their widespread adoption is constrained by expensive instrumentation and relatively low sensitivity. While ECL boasts high sensitivity and selectivity, the complexity of designing efficient luminophore-co-reactant pairs [23, 24], coupled with the difficulty in controlling short-lived radicals within complex matrices, presents a significant barrier to multiplexed miRNA detection.

LSPR is a resonance phenomenon caused by the absorption of specific wavelengths of light by metal nanoparticles [25]. It has been widely used in label-free small molecule detection due to its high sensitivity and low background noise. Currently, various LSPR sensing strategies have been proposed to enhance detection sensitivity by altering the material and morphology of metal nanoparticles [26–28]. However, these approaches struggle to achieve improvements spanning multiple orders of magnitude. Due to the extremely low concentration of miRNA in blood and fecal samples, LSPR technology is often combined with signal amplification strategies for miRNA detection, such as catalytic hairpin assembly (CHA) [29–31], and hybridization chain reaction (HCR) [32–34]. At the same time, the general sensing framework based on AuNP functionalization with DNA probes, target recognition via hybridization, and plasmonic readout has already been established in previous miRNA biosensing studies, including AuNP-based plasmonic systems relying on DNA-miRNA hybridization [33, 35–37]. Although these strategies greatly enhance detection sensitivity, they often introduce false positives and increase assay complexity, which can complicate quantitative analysis in complex biological matrices. Consequently, achieving both high sensitivity and reliable amplification-free quantitative detection remains a significant challenge in the field of miRNA detection.

In situ detection, as a commonly used strategy in analytical detection, can significantly enhance measurement reliability. In spectroscopic detection and analysis technology, in situ detection refers to the spectroscopic analysis of the same population of metal nanoparticles before and after a detection event. This design aims to eliminate spatial sampling errors. By fixing the nanoparticle population within the observation field of view, the shift in the plasmon resonance peak position can be precisely recorded, thereby achieving high-precision quantification of biomolecular binding events. This strategy effectively avoids the statistical bias inherent in conventional detection methods caused by the distributional heterogeneity of nanoparticles across different fields of view, significantly improving the reliability of the detection results. This strategy has been widely applied to SERS [38–40], Surface Plasmon Resonance (SPR) [41–43], and LSPR [44–46] technologies. However, few studies have combined in situ detection strategies with LSPR technology for miRNA detection.

Herein, we introduce an in situ single-particle plasmonic assay for the in situ detection of miR-451, leveraging the LSPR of individual AuNPs within a microfluidic environment (Scheme 1). This system is architected around a tri-layer microfluidic chip,

comprising hydroxy- and amino-functionalized SiO_2 substrates sandwiching a patterned polydimethylsiloxane (PDMS) layer that defines the flow channel. The sensing elements consist of AuNPs functionalized with two distinct thiolated DNA probes: a capture probe (probe 1) and a hairpin-structured recognition probe (probe 2). The detection mechanism is initiated by the specific hybridization of target miR-451 with probe 2 via a strand displacement reaction, which subsequently facilitates the conjugation of the activated probe 2 to probe 1. The hybridization-mediated AuNP sensing chemistry used here is therefore not fundamentally new; rather, the principal innovation of our methodology lies in the in situ tracking of the same immobilized nanoparticles before and after target exposure, together with a statistical readout at single-particle resolution. Conventional LSPR-based assays typically quantify the average LSPR peak shift across a population of nanoparticles within a given field of view (FOV), an approach susceptible to spatial sampling errors due to FOV inconsistencies. In contrast, our platform immobilizes probe 1-conjugated AuNPs within the microfluidic channel via electrostatic interactions with the amino-functionalized surface. This permits longitudinal tracking of the LSPR spectrum from the same set of individual AuNPs before and after the introduction of both probe 2-conjugated AuNPs and the sample. The presence of miR-451 induces nanoparticle aggregation, manifesting as a characteristic LSPR redshift. Critically, the target concentration is derived from the percentage of individual AuNPs that exhibit a significant spectral shift, rather than the mean shift amplitude of a heterogeneous population. This paradigm shift from ensemble averaging to a digital-like statistical readout at the single-particle level effectively circumvents spatial sampling variability. Consequently, our amplification-free assay achieves exceptional sensitivity for miR-451, with a measured limit of detection (LOD) of 58 fM, underscoring its potential for direct, ultrasensitive miRNA profiling.

2 | Experimental

2.1 | Materials and Reagents

Sulfuric acid (H_2SO_4, 98%, FUCHEN), Hydrogen peroxide (H_2O_2, 37%, DAMAO), 3-Aminopropyl trimethoxysilane (APTMS, 97%, MAKLIN), N-2-Hydroxyethylpiperazine-N'-2-ethane sulfonic acid (HEPES, 1 M, PH 7, YUANYE), Sodium Citrate Buffer (0.1 M, PH 3, MAKLIN), Polydimethylsiloxane (PDMS, HEOWNS). Tris (2-carboxyethyl) phosphine (TCEP, Takara), microRNA-451 (miR-451, Sangon Biotech), single−stranded DNA (ssDNA, Sangon Biotech), bovine serum(Dingguo), $MgCl_2$ buffer(25 mM, DNase, RNase & Protease free, Sterile, Coolaber), KAc (3 M, PH 5.5, DNase, RNase &Protease free, Sterile, Beyotime), Tris-HCl (1 M, PH 8.0, DNase, RNase &Protease free, Sterile, Beyotime), NaCl (5 M, DNase, RNase &Protease free, Sterile, Beyotime), DEPC water (DNase, RNase &Protease free, Sterile, Beyotime).

2.2 | Preparation of AuNPs and Surface Functionalization of SiO_2

AuNPs with a diameter of 50 nm were synthesized via the sodium citrate reduction method. Initially, 1% chloroauric acid ($HAuCl_4$) solution was slowly added dropwise to 100 mL of ultrapure water (18.2 MΩ·cm) under continuous magnetic stirring, followed by heating the mixture to 95°C. Subsequently, 350 mL of sodium citrate solution was rapidly injected into the reaction mixture. Within 2 min, the solution exhibited a distinct color change. The reaction was maintained under continuous magnetic stirring and heating for an additional 20 min. It is important to note that all equipment and vessels used during the synthesis must be carefully cleaned to prevent contamination, as impurities can lead to non-uniform particle size distribution in the synthesized AuNPs.

36 mL of a 37% H_2O_2 solution was slowly added to 84 mL of a 98% H_2SO_4 solution using a glass rod to prepare the piranha solution. The SiO_2 sheets, previously cleaned with deionized water and ethanol, were immersed in the piranha solution for 30 min to introduce hydroxyl groups(-OH) onto their surfaces. Following hydroxylation, the SiO_2 sheets were subjected to ultrasonic cleaning three times in deionized water and ethanol, and then divided into two groups: Group A and Group B. Group A, intended for the top layer of the microfluidic chip, was not further treated, while Group B, intended for the bottom layer of the chip, underwent amino functionalization. The SiO_2 sheets from Group B were immersed in a 1% APTMS (3-aminopropyltriethoxysilane) solution in ethanol for 30 min, followed by three cycles of ultrasonic cleaning in ethanol and deionized water. Finally, the SiO_2 sheets were heated at 120°C for 2 h. The methyl group in APTMS undergoes hydrolysis, forming hydrogen bonds with the hydroxyl groups on the SiO_2 surface. Upon heating, stable Si—O bonds are formed.

2.3 | Fabrication of the Microfluidic Chip

The PDMS prepolymer and curing agent were mixed at a 10:1 ratio and thoroughly stirred. The mixture was then poured onto a microfluidic template and heated at 80°C for 30 min to fabricate the PDMS channels. Afterward, the PDMS channels were subjected to plasma treatment for 30 s to introduce -OH groups onto the PDMS surface. SiO_2 sheets from Groups A and B were then attached to the top and bottom surfaces of the PDMS channels, followed by heating at 120°C for 2 h. The bonded PDMS-SiO_2 assemblies were left at room temperature for 24 h to allow for full bonding. The microfluidic chip consisted of a central circular sensing chamber (2 mm in diameter) connected to inlet and outlet channels (500 μm in width and 2 cm in length) with a channel height of 50 μm. During the assay, the solution was introduced using a microfluidic pump at a flow rate of 6 mL h^{-1}. Detailed structural views and COMSOL simulation results are provided in Figures S1 and S2.

2.4 | Preparation of AuNPs-ssDNA

Based on the principle of complementary base pairing, ssDNA sequences were designed and named probe 1 and probe 2, respectively (Table S1). The purchased probe 2 was a linear single-stranded DNA. To convert it into a stem-loop (hairpin) structure, it was first dissolved in DEPC-treated water to a concentration of 10 μM. The solution was then heated to 95°C for 4 min, followed by annealing to room temperature at a rate of 1°C/min. This procedure facilitated the spontaneous folding of the single

-stranded probe into its hairpin conformation. To prepare the functionalized AuNPs, 2.5 μL of 10 μM probe 1 and 15 μL of 100 μM mismatched DNA (mis-DNA) (molar ratio of 1:60) were mixed, followed by the addition of 5 μL of 0.5 M TCEP. The mixture was incubated at room temperature for 30 min to activate the thiol groups. Similarly, 15 μL of 10 μM probe 2 and 15 μL of 100 μM mis-DNA (molar ratio of 1:10) were mixed, with 10 μL of 0.5 M TCEP added to activate the thiol groups under the same conditions. Subsequently, 730 μL of 75 pM AuNPs was added to each mixture, and the samples were frozen at −20°C for 2 h. Successfully conjugated AuNPs-ssDNA exhibit a purple-red color upon thawing. If the sample appears colorless with black precipitates, it indicates that the AuNPs have aggregated. After thawing, the samples were centrifuged at 4000 rpm, and the precipitates were resuspended in DEPC-treated water.

2.5 | In Situ Detection of miR-451

3 μL of sodium citrate buffer (pH 3) was mixed with 27 μL of AuNPs-probe 1 and introduced into the microfluidic chip at a flow rate of 60 μL/h for 30 min. The acidic condition provided by the sodium citrate buffer enhances the electrostatic adsorption of AuNPs onto the amine-functionalized bottom surface of the microfluidic chip. Additionally, the citrate ions present in the AuNPs synthesis process prevent the introduction of impurities. After incubation, deionized water was flowed through the microfluidic chip to remove any unbound AuNPs-probe 1.

The 2× buffer (10 mL final volume) was prepared by combining 200 μL of 1 M Tris-HCl, 200 μL of 5 M NaCl, 4 mL of 25 mM $MgCl_2$, and 5.6 mL of DEPC-treated water. Simultaneously, 1 μL of 10 μM miR-451 was mixed with 40 μL of AuNPs-probe 2 and 50 μL of 2×buffer, resulting in a final miR-451 concentration of 100 nM. The mixture was incubated at 55°C for 30 min to ensure hybridization of miR-451 with AuNPs-probe2.

The microfluidic chip, adsorbed with AuNPs-probe 1 was analyzed using a dark-field microscope. Subsequently, the AuNPs-probe2-miR-451 complex was introduced into the microfluidic chip and incubated at 55°C for 1 h. Finally, the chip was washed with deionized water to remove any unbound complexes and was subsequently analyzed. Thus, the total analytical detection time, including AuNPs-probe 1 immobilization (30 min), target hybridization with AuNPs-probe 2 (30 min), and in-chip incubation (1 h), was within 2 h, and the overall sample-to-readout process was completed within 3 h. It should be noted that this analytical time does not include chip fabrication or surface pretreatment steps, which can be performed in advance.

2.6 | Statistical Analysis

For quantitative analysis of miR-451 at different concentrations, three repeated measurements were performed for each concentration. In each measurement, approximately 800–1000 AuNPs were analyzed, depending on the concentration group. The response percentage was determined from the classified AuNP populations. Data are presented as mean ± standard deviation (SD) unless otherwise noted. The mean and SD values were calculated from the three repeated measurements at each concentration and therefore reflect variability among repeated measurements rather than particle-to-particle variation within a single image. Error bars in the calibration plots represent SD from three repeated measurements. Detailed particle-counting statistics for each concentration are provided in Table S2. Data processing and plotting were performed using MATLAB 2024a and Origin 2018.

3 | Results and Discussion

3.1 | Determination of the Optimal Size of AuNPs

To determine the optimal size of AuNPs for LSPR sensing applications, the LSPR scattering cross-sections of both single AuNP and AuNP dimers with diameters ranging from 10 to 70 nm were systematically simulated using Lumerical FDTD software. The scattering peak wavelength of single AuNP exhibited a moderate redshift as their diameter increased (Figure 1a), while AuNP dimers demonstrated a more pronounced redshift in their scattering peaks with increasing size (Figure 1b). Additionally, the scattering cross-sections of both single AuNP and AuNP dimers were observed to increase with particle size. The selection of AuNP size constitutes a trade-off between scattering intensity and spectral resolution. Smaller AuNPs exhibit lower scattering peak intensity and a lower signal-to-noise ratio, making their detection more susceptible to noise in microscopy imaging. In contrast, larger AuNPs provide a higher signal-to-noise ratio but possess a broader full width at half maximum (FWHM), which compromises the accuracy of identifying spectral redshift. Furthermore, to align with the optimal quantum efficiency range (450–600 nm) of the camera, AuNPs with a diameter of 50 nm were selected as the optimal configuration for the LSPR sensor. Furthermore, AuNP dimers exhibited significantly stronger electric field intensities compared to single AuNP (Figure 1c,d). Therefore, normalization of the spectra before and after testing is required for accurate analysis of AuNP spectral responses.

3.2 | Characterization of AuNPs-ssDNA

To prevent nonspecific dimeric aggregation of the gold nanoparticles (AuNPs), the particle surface was functionalized with an excess of thiol-modified ssDNA to promote the formation of a protective DNA layer. The hydrodynamic diameters of both AuNPs and AuNPs-ssDNA were characterized using dynamic light scattering (DLS) (Figure 2a). The average diameter of the AuNPs was measured to be 50.748 nm, while that of the AuNPs-ssDNA increased to 68.061 nm. The designed 27-base ssDNA has a length of approximately 8.9 nm (with a single base length of about 0.33 nm), and the 17.3 nm increase in diameter was consistent with the formation of a surface-bound DNA layer on the AuNPs. Additionally, the zeta potentials of AuNPs and AuNPs-ssDNA were characterized to provide additional evidence for ssDNA modification of the AuNP surface. The citrate-stabilized AuNPs, which carry citrate anions on their surface, exhibited a zeta potential of −30.6 mV. Following ssDNA modification, the zeta potential shifted to −36.4 mV (Figure 2b), which is consistent with the increased surface electronegativity introduced by the negatively charged phosphate backbone of ssDNA.

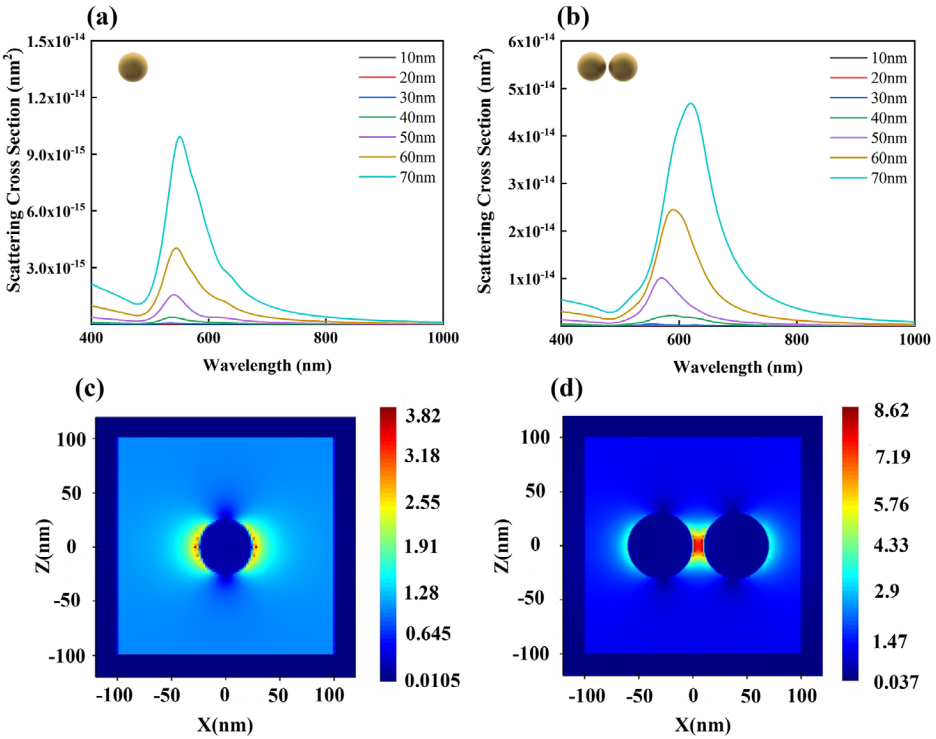

FIGURE 1 | (a) Relationship between scattering cross-section and diameter of single AuNP. (b) AuNP dimers. (c) Simulation of the electric field of a single AuNP. (d) AuNP dimers.

The absorption spectra of AuNPs and AuNPs-ssDNA were measured using a spectrophotometer. Both AuNPs and AuNPs-ssDNA were centrifuged at 4000 rpm for 20 min, and the precipitates were resuspended in deionized water. The absorption spectra of AuNPs and AuNPs-ssDNA were then recorded (Figure 2c). The citrate-reduced AuNPs displayed a characteristic absorption peak at 531 nm. In comparison, the absorption spectrum of AuNPs-ssDNA exhibited a 3 nm redshift, which is consistent with the presence of a DNA coating that changes the local refractive index surrounding the AuNPs.

To further support thiol-mediated functionalization of AuNPs, a controlled freezing assay was conducted with thiolated and non-thiolated DNA, respectively (Figure S3). After thawing, the mixture containing thiolated DNA and AuNPs remained a homogeneous wine-red solution. In contrast, the mixture with non-thiolated DNA became colorless and formed a black precipitate. Citrate-capped AuNPs possess a negative zeta potential in water, leading to electrostatic repulsion that prevents aggregation. During the freezing process, as water turns to ice, both AuNPs and DNA are concentrated into the interstitial spaces, forcing them into close proximity. For thiolated DNA, this proximity facilitates stable surface anchoring to AuNPs, which is consistent with thiol-mediated binding and helps generate a protective DNA layer that suppresses aggregation even when particles are brought into close contact. For non-thiolated DNA, however, no comparable stable attachment is expected. The absence of a protective layer allows the concentrated AuNPs to aggregate irreversibly upon close contact.

The stability of the DNA-functionalized AuNPs was further assessed under high-salt conditions. A 100 mM NaCl environment was created by adding 100 μL of 1 M NaCl to 900 μL of as-synthesized citrate-AuNPs or thiolated ssDNA-AuNP conjugates. The unmodified citrate-AuNPs aggregated immediately upon salt addition, forming a visible precipitate (Figure S4a). This is because the high salt concentration screens the negative surface charge, eliminating the electrostatic repulsion that stabilizes the pristine AuNPs. The resulting aggregate could not be re-dispersed even with sonication. In contrast, the thiolated ssDNA-AuNP conjugates settled gradually over time (Figure S4b). Crucially, this settlement was reversible; gentle vortexing was sufficient to re-disperse the particles into a homogeneous solution (Figure S4c). Although the screened electrostatic force allows the DNA-capped particles to approach each other, the steric hindrance and stability provided by the covalently bound DNA monolayer prevent irreversible aggregation. The settling is attributed to gravitational forces over time, and the particles can be easily re-suspended. This result demonstrates the improved colloidal stability of the ssDNA-AuNP conjugates in high-salt environments.

AuNPs and AuNPs-ssDNA were immobilized on amine-functionalized silica substrates for XPS characterization. The Au 4f binding energy of citrate-reduced AuNPs was measured at 84.05 eV (Figure 2d). After treatment with thiolated ssDNA, a negative shift of 0.48 eV was observed in the Au 4f spectrum, indicating a change in the surface chemical environment of the AuNPs that is consistent with DNA functionalization. This shift originates from the evolution of surface chemistry: Citrate-synthesized AuNPs initially adsorb citrate anions via Au-O (carboxyl) coordination, which explains their inherent negative zeta potential. When thiolated ssDNA is introduced to the AuNP surface, thiol-mediated binding is expected to alter the original surface coordination environment and thereby

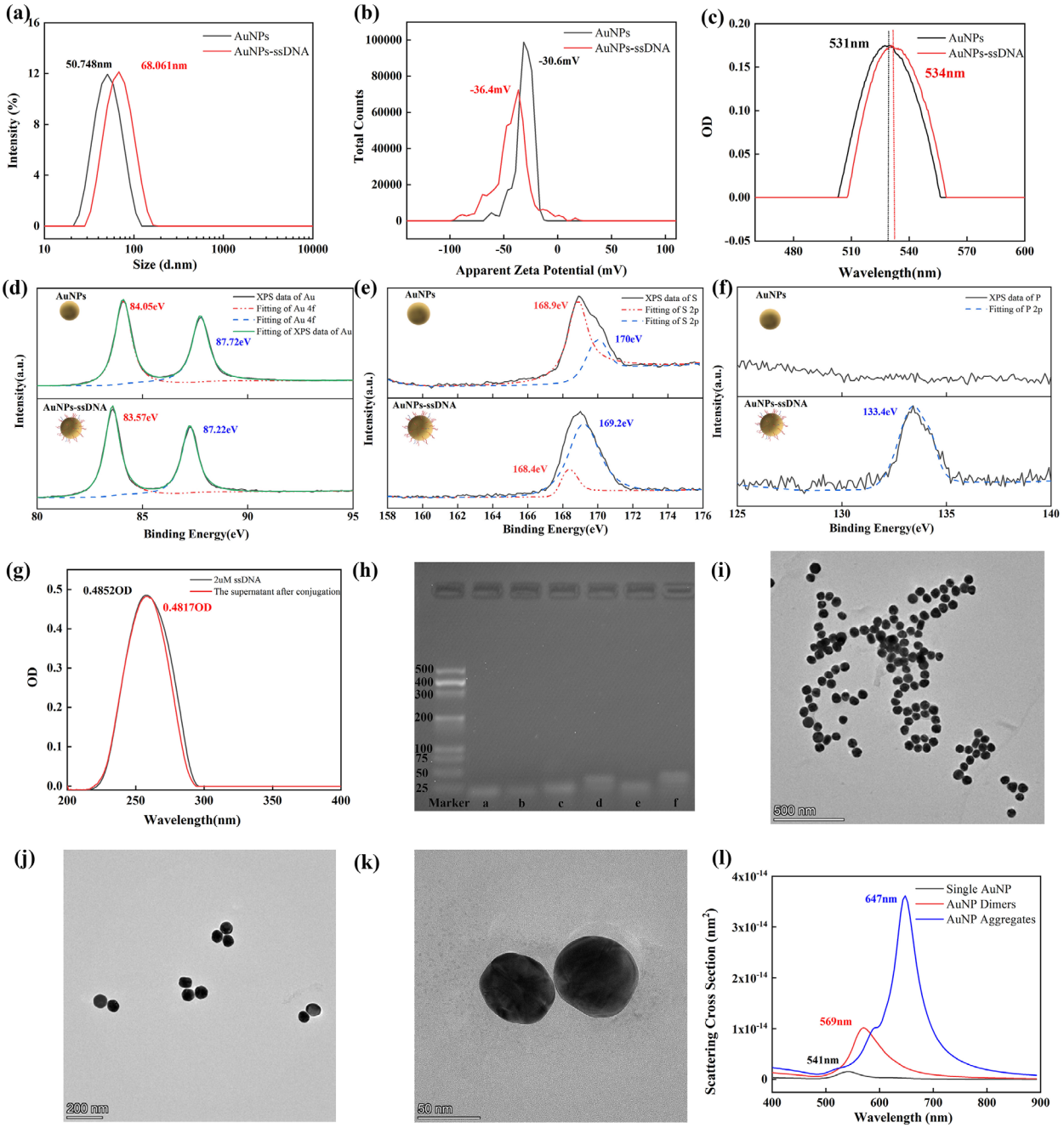

FIGURE 2 | Characterization of AuNP–ssDNA conjugates and probe-mediated AuNP binding behavior. (a) Hydrodynamic diameter distributions of AuNPs and AuNPs-ssDNA measured by DLS. (b) Zeta potentials of AuNPs and AuNPs-ssDNA. (c) UV–vis absorption spectra of AuNPs and AuNPs-ssDNA. (d) XPS spectra of the Au 4f region for citrate-stabilized AuNPs and AuNPs-ssDNA conjugates. (e) XPS spectra of the S 2p region. (f) XPS spectra of the P 2p region. (g) UV–vis absorption spectra of 2 μM ssDNA and the corresponding supernatant after conjugation with AuNPs using the freezing-assisted method. (h) Agarose gel electrophoresis analysis of hybridization among miR-451, probe 1, and hairpin probe 2. Lanes: a, 2 μM miR-451; b, 2 μM probe 1; c, 2 μM hairpin probe 2; d, 2 μM hairpin probe 2 + miR-451; e, 2 μM probe 1 + hairpin probe 2; f, 2 μM miR-451 + probe 1 + hairpin probe 2. (i) TEM image of AuNPs modified with probe 1 and probe 2 after miR-451 addition. (j) TEM image of AuNPs modified with mis-DNA and probe 1 at a molar ratio of 60:1, and with mis-DNA and probe 2 at a molar ratio of 10:1 after miR-451 addition. (k) Magnified view of the dimer structure in (j). (l) FDTD-simulated LSPR scattering spectra of a single AuNP, an AuNP dimer, and an AuNP aggregate.

change the electronic state of surface Au atoms. The lower electronegativity of sulfur ($\chi = 2.58$) compared to oxygen ($\chi = 3.44$) reduces electron withdrawal from Au atoms, while sulfur's lone electron pairs may donate partial electron density to the Au surface. These synergistic effects collectively increase the electron density around Au atoms, thereby lowering the binding energy required for Au 4f photoelectron emission. The XPS spectrum of the S 2p region exhibited a peak at approximately 169 eV, which is attributed to sulfur in sulfate ions (SO_4^{2-}) rather than thiolated ssDNA (Figure 2e). This observation is consistent with residual sulfate ions from the piranha solution treatment used for hydroxylation of the SiO_2 surface. Theoretically, sulfur

derived from thiolated ssDNA would be expected to appear near 162 eV in the S 2p region; however, due to the extremely low sulfur content of the DNA probes, no distinct thiol-derived S 2p signal could be reliably resolved in our measurements. The presence of P provided direct evidence for the presence of DNA on the AuNP-modified surface (Figure 2f). When AuNPs alone were immobilized on the SiO_2 surface, no P 2p signal was detected, as expected in the absence of DNA. In contrast, after immobilization of AuNPs-ssDNA conjugates, a distinct P 2p peak emerged at 133.4 eV, corresponding to phosphorus in the phosphate backbone of ssDNA. To determine the conjugation efficiency, a solution containing 2 μM thiolated ssDNA and 73.5 pM AuNPs was prepared by mixing 15 μL of 100 μM ssDNA with 735 μL of 75 pM AuNPs. The conjugation was facilitated using a freeze-assisted method. Following conjugation, the mixture was centrifuged, and the absorption spectrum of the supernatant was measured and compared to that of the initial 2 μM ssDNA solution (Figure 2g). The initial ssDNA solution (2 μM) exhibited an absorbance of 0.4852 OD at 260 nm. The absorbance of the supernatant after conjugation was measured to be 0.4817 OD at the same wavelength. The decrease in absorbance ($\Delta OD = 0.0035$) corresponds to the concentration of ssDNA estimated to have been associated with the AuNPs after the conjugation process. Based on the Beer-Lambert law, this absorbance difference equates to a bound ssDNA concentration of approximately 15 nM. Consequently, the molar ratio of thiolated ssDNA bound to AuNPs was calculated to be 204: 1.

Taken together, these results support successful DNA functionalization of the AuNPs. However, the evidence for Au–S bonding remains indirect, because a distinct thiol-derived S 2p signal was not clearly resolved in the XPS measurements. Therefore, the surface modification was inferred from the combined physicochemical characterization, control experiments, and DNA loading analysis, rather than from the S 2p spectrum alone.

3.3 | Characterization of AuNPs Binding

The hybridization events among probe 1, probe 2, and miR-451 were characterized using agarose gel electrophoresis (Figure 2h). Lanes a, b, and c correspond to 2 μM of miR-451, probe 1, and hairpin probe 2, respectively, serving as reference markers. Lane d shows the product after incubating 2 μM hairpin probe 2 with miR-451 at 55°C in 1X buffer for 30 min. The observed upward band shift compared to lanes a and c confirms the successful hybridization between hairpin probe 2 and miR-451.Lane e represents the mixture of 2 μM hairpin probe 2 and probe 1 under the same incubation conditions. The lack of a band shift compared to lanes b and c verifies that no hybridization occurs between probe 1 and hairpin probe 2 in the absence of the target. Lane f displays the result of incubating a mixture of 2 μM Probe 1, hairpin probe 2, and miR-451. A more pronounced band shift is observed compared to all other lanes, demonstrating the successful formation of the ternary complex involving probe 1, probe 2, and miR-451.

The surfaces of AuNPs were functionalized with probe 1 and mis-DNA at a molar ratio of 1:60, and with probe 2 and mis-DNA at a molar ratio of 1:10. This functionalization strategy was specifically designed to reduce the proportion of effective DNA on the AuNP surface. When AuNPs were exclusively functionalized with probe 1 and probe 2, a single probe 1-functionalized AuNP frequently bound multiple probe 2-functionalized AuNPs, resulting in the formation of aggregated clusters (Figure 2i). Minimizing the number of AuNPs bound to a single nanoparticle was critical in situ detection for improving the accuracy of miRNA quantification. This accuracy was achieved by calculating the ratio of AuNPs exhibiting LSPR shifts to all AuNPs. However, when AuNPs form aggregates, a single LSPR redshift event could originate from either a dimer or an aggregate, which would significantly compromise quantification accuracy if not distinguished. To minimize errors, it was crucial to decrease the proportion of effective DNA on the AuNP surface to limit the formation of clusters of aggregated AuNPs. TEM images demonstrated that reducing the effective DNA proportion substantially mitigated the formation of aggregated clusters of AuNPs (Figure 2j,k). This result verified that the AuNPs were connected via the specific hybridization mechanism of probe 1-miR-451-probe 2, rather than by nonspecific aggregation.

Although the majority of the aggregates are dimers, a small population of aggregates consisting of three AuNPs may still form. To establish objective classification criteria, we performed finite-difference time-domain (FDTD) simulations of the LSPR scattering spectra for a single 50-nm AuNP, a dimer, and an aggregate of three AuNPs (Figure 2l). The simulated scattering peaks were located at 541, 569, and 647 nm, respectively. Based on these simulation results, we defined the following thresholds for classifying the spectral shifts of individual AuNPs: A redshift of less than 10 nm was considered an invalid point (no specific binding). A redshift between 10 and 40 nm was classified as a dimer. A redshift greater than 40 nm was classified as an aggregate of three AuNPs. The percentage of redshifted AuNPs was then calculated using the following formula, which specifically accounts for effective dimers to ensure accurate quantification:

$$P = \frac{n_1 + kn_2}{N} \times 100\% \quad (1)$$

In this formula, P represents the aggregation percentage; N is the total number of AuNPs analyzed in the field of view; n_1 is the number of points classified as dimers; n_2 is the number of points classified as aggregates of three AuNPs; k is a weighting factor with a value of 2, accounting for the greater signal contribution from an aggregate compared to a dimer.

3.4 | Characterization of Electrostatic Adsorption of AuNPs

The adsorption density of AuNPs on amino-functionalized SiO_2 surfaces depended on the adsorption time. AFM was used to characterize the electrostatic adsorption of AuNPs on the amino-modified SiO_2 surfaces after 3, 2, and 1 h (Figure 3a–c). The results indicated that the adsorption density of AuNPs gradually increased as the adsorption time was extended. In addition, the uniformity of the prepared gold nanoparticles was confirmed (Figure 3d). As the adsorption density of AuNPs increased, the color of the SiO_2 substrates gradually changed from pale pink to purple-red (Figure S5).

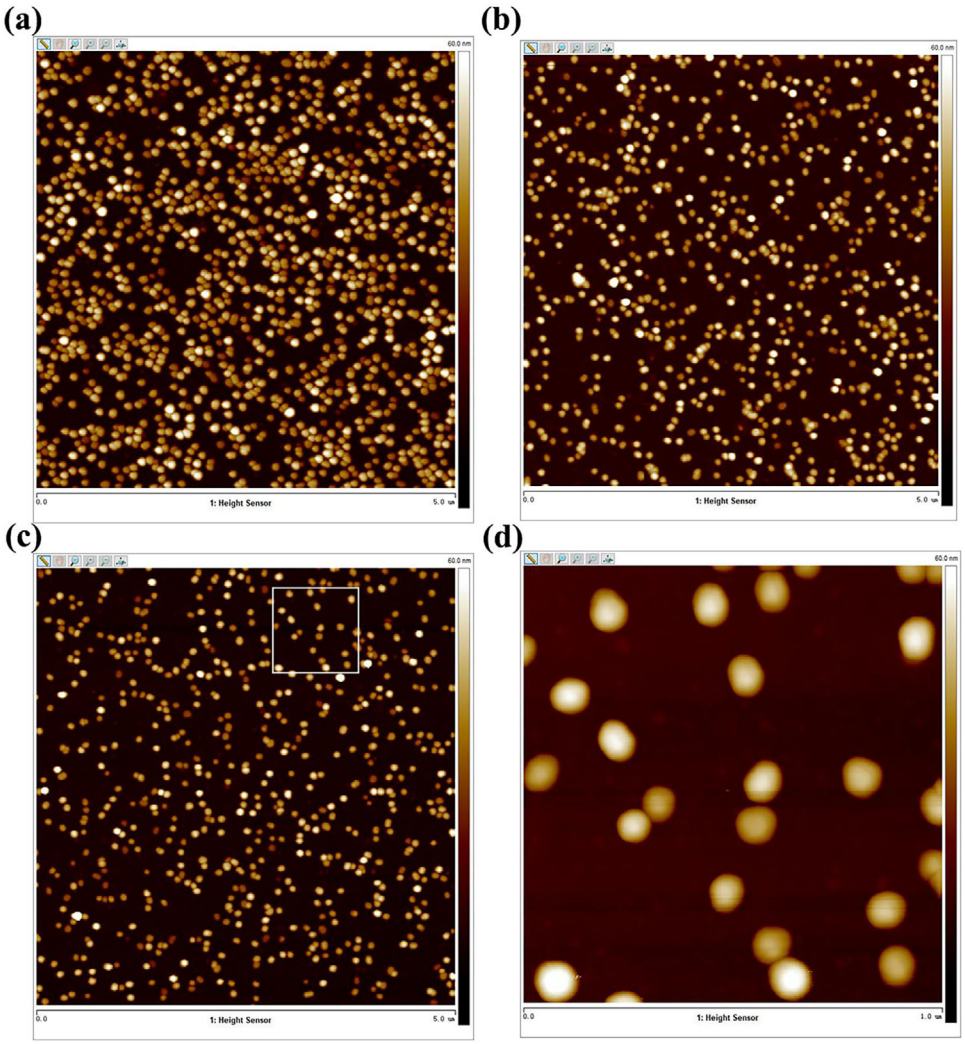

FIGURE 3 | (a) AFM image of AuNPs electrostatically adsorbed on SiO_2 surface for 3 h; (b) adsorption for 2 h; (c) adsorption for 1 h; (d) enlarged view of the white-boxed region in (c).

3.5 | Dark-Field Detection of miR-451

The scattering intensity of AuNPs under 400–600 nm incident light was recorded using dark-field microscopy with an in situ detection strategy, and the spectra from both measurements were analyzed. When AuNPs-probe 1 did not bind to AuNPs-probe 2 via hybridization with miR-451, no change was observed in the LSPR peaks in both spectra (Figure 4a). When AuNPs-probe 1 bound to AuNPs-probe 2 through hybridization with miR-451, a redshift in the LSPR peak was observed in the second spectrum (Figure 4b). It is important to note that in Figure 4a,b, the *x*-axis represented the wavelength of the incident light, while the *y*-axis represented the scattering intensity of the particles. This was because the dark-field microscope utilized a monochrome camera capable of detecting only the scattering light intensity, without analyzing the wavelength of the scattered light. Therefore, the *x*-axis corresponded to the incident light wavelength modulated by the monochromator in the scattering intensity spectrum.

To detect miR-451 at varying concentrations, different concentrations of miR-451 were introduced into the microfluidic channel. The proportion of AuNPs exhibiting a redshift in their spectra relative to the total AuNPs was analyzed before and after introducing miR-451. Theoretically, any miR-451 present should induce spectral changes in some particles within the dark-field view, indicating that this detection method has an extremely low detection limit.

Dark-field microscopy was used to detect miR-451 at concentrations of 100 fM, 1, 10, 100 pM, 1, 10, and 100 nM, and the spectra were analyzed. The percentage of AuNPs exhibiting redshift in the LSPR peaks was fitted (Figure 4c). The limit of detection (LOD) was calculated to be 58 fM based on the mean blank signal ($n = 3$) plus three times the standard deviation. The statistical results for the blank sample and different concentrations of miR-451 are summarized in Table S2. The main challenge in achieving the theoretically low detection limit arises from the difficulty of the ssDNA modified on the surface of AuNPs in pulling larger AuNPs, resulting in greater randomness in the base pairing activity between AuNPs-probe1 and AuNPs-probe2-miR-451. Compared with representative reported amplification-free miRNA detection methods, our strategy shows a competitive

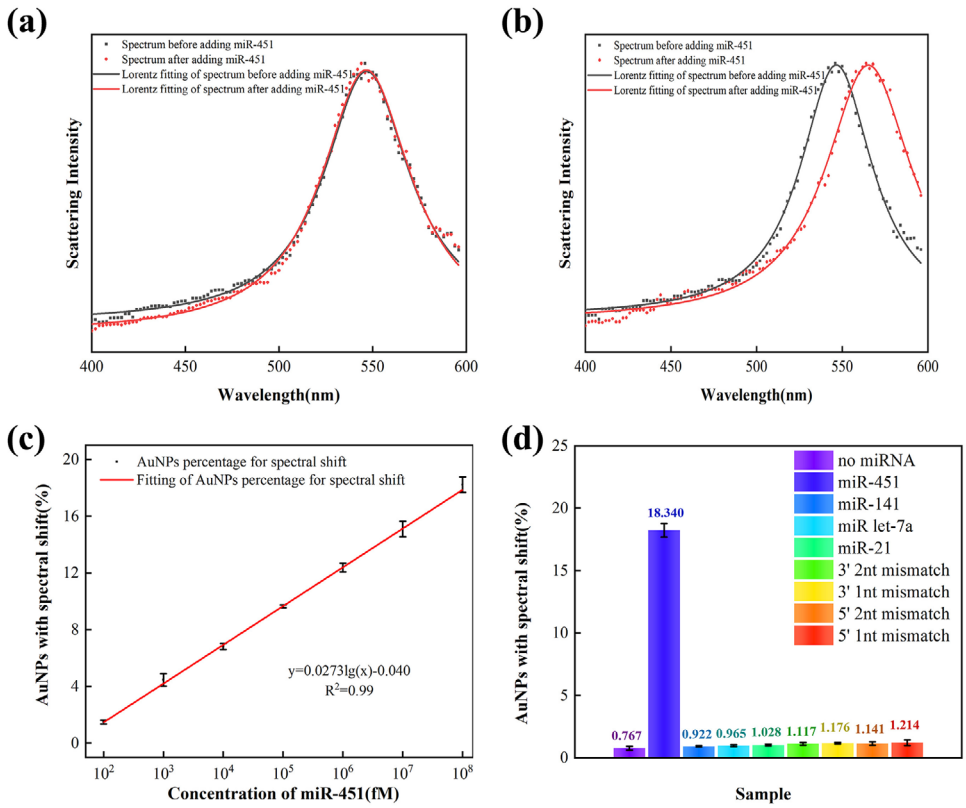

FIGURE 4 | (a) In situ detection spectra of AuNPs-probe 1 without hybridization with miR-451 and AuNPs-probe 2; (b) In situ detection spectra of AuNPs-probe 1 hybridized with miR-451 and AuNPs-probe 2; (c) Fitting curve for in situ detection of miR-451 at concentrations ranging from 100 fM to 100 nM; (d) Detection results of blank samples, miR-451, miR-141, miRNA let-7a, miR-21, 3‘ 2 nt mismatch, 3‘ 1 nt mismatch, 5‘ 2 nt mismatch and 5‘ 1 nt mismatch at a concentration of 100 nM, showing discrimination of the fully matched target from non-target miRNAs and closely related single-/double-mismatched sequences. Each data point represents mean ± SD from three repeated measurements ($n = 3$). Error bars represent SD. Detailed particle-counting statistics are provided in Table S2.

detection limit while additionally offering an in situ single-particle statistical readout and applicability in spiked serum samples (Table S4). Although the assay time is not the shortest among reported methods, the fixed-particle tracking format provides improved measurement robustness by analyzing the same AuNP population before and after target recognition.

To further support the simulation-guided spectral classification, AFM characterization was performed on the AuNP-modified substrate under 0 M and 100 nM miR-451 conditions. As shown in Figure S7, the surface was mainly occupied by isolated AuNPs in the absence of miR-451, whereas dimer and aggregate features became observable after the addition of 100 nM miR-451. In the representative 3 × 3 μm^2 AFM image after target addition, two dimer features and one aggregate feature were identified, corresponding to a weighted percentage of 17.4% according to Equation (1). These AFM results provide orthogonal morphological support for the target-induced nanoparticle aggregation inferred from the LSPR redshift.

To further evaluate the robustness of the assay, chip-to-chip, batch-to-batch, and day-to-day reproducibility tests were performed at 10 pM and 1 nM miR-451. As shown in Figure S8, the responses were highly consistent under all three conditions, with all RSD values below 5% (Table S3), indicating good reproducibility of the proposed assay.

To better interpret the analytical significance of this concentration-based LOD, we further estimated the corresponding target copy number using $N = C \times V \times N_A$, where C is the target concentration, V is the assay volume, and N_A is Avogadro’s constant. Based on the measured LOD of 58 fM and the assay volume of 1 μL miR-451 used in the present microfluidic chamber, the corresponding number of miR-451 molecules is approximately 3.5×10^4 copies. This result supports the feasibility of amplification-free miRNA detection under the present assay conditions. However, this concentration-based LOD should not be overinterpreted as demonstrating clinical equivalence to amplification-based techniques such as RT-qPCR, because practical performance in clinical samples also depends on matrix effects, sample processing, and benchmarking against established reference methods.

The specificity of the assay was evaluated by testing a blank sample, 100 nM of miR-451, and both non-target and closely related sequences, including miR-141, let-7a, miR-21, as well as miR-451 variants with single- and double-base mismatches at the 5’ end (5’ 1 nt mismatch, 5’ 2 nt mismatch) and 3’ end (3’ 1 nt mismatch, 3’ 2 nt mismatch) (Figure 4d). This design allowed us to directly assess the ability of the assay to discriminate the fully matched target from unrelated miRNAs as well as from closely related single-/double-mismatched sequences under the tested conditions. The signal intensities for miR-141, miR-21, and let-7a

TABLE 1 | Analytical results for the detection of miR-451 in bovine serum ($n = 5$).

Sample	Added	Group 1	Group 2	Group 3	Recovery (%)	RSD (%)
1	100fM	80.55 fM	98.24 fM	112 fM	96.93	16.26
2	1pM	0.95 pM	0.95 pM	1.11 pM	100.33	9.25
3	10pM	10.96 pM	9.86 pM	10.17 pM	103.3	5.49
4	100pM	99.78 pM	98.1 pM	107.5 pM	101.79	4.92
5	1nM	0.96 nM	1.07 nM	0.97 nM	100	6.08
6	10nM	10.45 nM	9.37 nM	9.81 nM	98.77	5.50

showed no significant difference compared to the blank control, whereas miR-451 produced a markedly higher signal response. Among the mismatch variants, the 5' single-base mismatch (5' 1 nt MM) yielded a slightly higher non-specific signal than the other homologous miR-451 variants. This is likely because a single mismatch at the 5' end can still partially open the hairpin structure of probe 2 to a small extent. Nevertheless, the response of the 5' 1 nt MM remained much lower than that of the perfectly matched miR-451, indicating effective mismatch discrimination by the assay. After subtracting the background signal, the CR% (Cross-reactivity Rate) was calculated to be 2.54%, demonstrating the strong selectivity of this in situ detection strategy for miR-451 and a low level of cross-reactivity under the tested conditions.

To validate the applicability of our in situ detection strategy in complex biological samples, we performed a spike-and-recovery experiment using bovine serum as a model for human blood. miR-451 was quantified in the serum matrix using the standard addition method. The results showed satisfactory recoveries ranging from 96.93% to 103.3%, with relative standard deviations (RSDs) between 4.92% and 16.26% (Table 1). These findings demonstrate the efficacy of our method for detecting miRNAs in serum. Although the RSD was relatively high at the 100 fM concentration, it remained within an acceptable range, confirming the robustness of the assay.

4 | Conclusion

This study presents an in situ single-particle miRNA detection strategy leveraging LSPR of AuNPs within a microfluidic chip. The primary advance of this work lies not in the general AuNP-DNA hybridization/plasmonic sensing mechanism itself, which has been widely explored in previous miRNA biosensing studies, but in the fixed observation of the same individual AuNPs before and after target hybridization. This design reduces spatial sampling errors inherent in conventional methods that average signals from transient nanoparticles. Probe-modified AuNPs were immobilized on the microfluidic channel surface via electrostatic adsorption. Upon specific hybridization with the target miR-451, the designed hairpin DNA probes induce AuNP aggregation. By quantifying the percentage of AuNPs that aggregate within a fixed field of view—rather than averaging spectral shifts—we achieved amplification-free, calibration-based quantitative detection of miR-451 with a detection limit of 58 fM. For the present assay volume of 1 μL, this LOD corresponds to approximately 3.5×10^4 target molecules, indicating the feasibility of amplification-free detection in the current platform. This direct quantitative approach bypasses nucleic acid amplification, thereby simplifying probe design (compared to methods like HCR and CHA) and avoiding the steps and potential errors associated with enzyme-free amplification techniques. Our amplification-free approach directly counts the binding events, providing a more direct and reliable correlation between the signal and the target concentration. Under the optimized protocol used in this study, the analytical in situ detection workflow can be completed within 3 h, although further simplification of the procedure will still be important for improving practical applicability. The successful detection in spiked bovine serum demonstrates feasibility in a model biological matrix, but does not yet establish clinical applicability for CRC diagnosis or screening. Further validation using clinical samples and direct comparison with established methods such as RT-qPCR will be necessary in future studies. In summary, this work provides a promising amplification-free strategy for the accurate and straightforward quantification of miRNA.

Acknowledgements

The authors were grateful for the financial support from the National Natural Science Foundation of China (62471256).

Conflicts of Interest

The authors declare no conflicts of interest.

Data Availability Statement

The data that support the findings of this study are available from the corresponding author upon reasonable request.

References

1. I. Mármol, C. Sánchez-de-Diego, A. Pradilla Dieste, E. Cerrada, and M. Rodriguez Yoldi, "Colorectal Carcinoma: A General Overview and Future Perspectives in Colorectal Cancer," *International Journal of Molecular Sciences* 18, no. 1 (2017): 197, https://doi.org/10.3390/ijms18010197.

2. G. Zhao, X. Liu, Y. Liu, et al., "Aberrant DNA Methylation of $SEPT_9$ and SDC_2 in Stool Specimens as an Integrated Biomarker for Colorectal Cancer Early Detection," *Frontiers in Genetics* 11 (2020): 11, https://doi.org/10.3389/fgene.2020.00643.

3. Y. Sano, J. S. Byeon, X. B. Li, et al., "Colorectal Cancer Screening of the General Population in East Asia," *Digestive Endoscopy* 28, no. 3 (2016): 243–249, https://doi.org/10.1111/den.12579.

4. B. Levin, D. A. Lieberman, B. McFarland, et al., "Screening and Surveillance for the Early Detection of Colorectal Cancer and Adenomatous Polyps, 2008: A Joint Guideline From the American Cancer Society, the

US Multi-Society Task Force on Colorectal Cancer, and the American College of Radiology," *Gastroenterology* 134, no. 5 (2008): 1570–1595, https://doi.org/10.1053/j.gastro.2008.02.002.

5. X. Pan, R. Wang, and Z. Wang, "The Potential Role of miR-451 in Cancer Diagnosis, Prognosis, and Therapy," *Molecular Cancer Therapeutics* 12, no. 7 (2013): 1153–1162, https://doi.org/10.1158/1535-7163.MCT-12-0802.

6. J. Ye, M. Xu, X. Tian, S. Cai, and S. Zeng, "Research Advances in the Detection of MiRNA," *Journal of Pharmaceutical Analysis* 9, no. 4 (2019): 217–226, https://doi.org/10.1016/j.jpha.2019.05.004.

7. M. Akmal, M. S. Baig, and J. A. Khan, "Suppression of Cotton Leaf Curl Disease Symptoms in Gossypium Hirsutum Through Over Expression of Host-Encoded MiRNAs," *Journal of Biotechnology* 263 (2017): 21–29, https://doi.org/10.1016/j.jbiotec.2017.10.003.

8. S. W. Kim, Z. Li, P. S. Moore, et al., "A Sensitive Non-Radioactive Northern Blot Method to Detect Small RNAs," *Nucleic Acids Research* 38, no. 7 (2010): 98, https://doi.org/10.1093/nar/gkp1235.

9. É. Várallyay, J. Burgyán, and Z. Havelda, "MicroRNA Detection by Northern Blotting Using Locked Nucleic Acid Probes," *Nature Protocols* 3, no. 2 (2008): 190–196, https://doi.org/10.1038/nprot.2007.528.

10. W. Li and K. Ruan, "MicroRNA Detection by Microarray," *Analytical and Bioanalytical Chemistry* 394, no. 4 (2009): 1117–1124, https://doi.org/10.1007/s00216-008-2570-2.

11. K. A. Cissell and S. K. Deo, "Trends in MicroRNA Detection," *Analytical and Bioanalytical Chemistry* 394, no. 4 (2009): 1109–1116, https://doi.org/10.1007/s00216-009-2744-6.

12. S. Mohammadi-Yeganeh, M. Paryan, S. Mirab Samiee, et al., "Development of a Robust, Low Cost Stem-Loop Real-Time Quantification PCR Technique for MiRNA Expression Analysis," *Molecular Biology Reports* 40, no. 5 (2013): 3665–3674, https://doi.org/10.1007/s11033-012-2442-x.

13. Y. Niu, L. Zhang, H. Qiu, et al., "An Improved Method for Detecting Circulating MicroRNAs With S-Poly(T) Plus Real-Time PCR," *Scientific Reports* 5, no. 1 (2015), https://doi.org/10.1038/srep15100.

14. G. A. Calin and C. M. Croce, "MicroRNA Signatures in Human Cancers," *Nature Reviews Cancer* 6, no. 11 (2006): 857–866, https://doi.org/10.1038/nrc1997.

15. Y. Wang, L. Zou, T. Wu, et al., "Identification of MRNA-MiRNA Crosstalk in Human Endothelial Cells after Exposure of $PM_{2.5}$ Through Integrative Transcriptome Analysis," *Ecotoxicology and Environmental Safety* 169 (2019): 863–873, https://doi.org/10.1016/j.ecoenv.2018.11.114.

16. V. Benes and M. Castoldi, "Expression Profiling of microRNA Using Real-Time Quantitative PCR, How To Use It and What is Available," *Methods* 50, no. 4 (2010): 244–249, https://doi.org/10.1016/j.ymeth.2010.01.026.

17. H. Zhang, X. Huang, J. Liu, and B. Liu, "Simultaneous and Ultrasensitive Detection of Multiple MicroRNAs by Single-Molecule Fluorescence Imaging," *Chemical Science* 11, no. 15 (2020): 3812–3819, https://doi.org/10.1039/D0SC00580.

18. B. Li, S. Yu, R. Feng, et al., "Dual-Mode Gold Nanocluster-Based Nanoprobe Platform for Two-Photon Fluorescence Imaging and Fluorescence Lifetime Imaging of Intracellular Endogenous MiRNA," *Analytical Chemistry* 95, no. 40 (2023): 14925–14933, https://doi.org/10.1021/acs.analchem.3c02216.

19. Y. Sun, L. Shi, L. Mi, R. Guo, and T. Li, "Recent Progress of SERS Optical Nanosensors for MiRNA Analysis," *Journal of Materials Chemistry B* 8, no. 24 (2020): 5178–5183, https://doi.org/10.1039/d0tb00280a.

20. Y. He, X. Yang, R. Yuan, and Y. Chai, "Switchable Target-Responsive 3D DNA Hydrogels as a Signal Amplification Strategy Combining With SERS Technique for Ultrasensitive Detection of MiRNA 155," *Analytical Chemistry* 89, no. 16 (2017): 8538–8544, https://doi.org/10.1021/acs.analchem.7b02321.

21. H. Rafiee-Pour, M. Behpour, and M. Keshavarz, "A Novel Label-Free Electrochemical MiRNA Biosensor Using Methylene Blue as Redox Indicator: Application to Breast Cancer Biomarker MiRNA-21," *Biosensors and Bioelectronics* 77 (2016): 202–207, https://doi.org/10.1016/j.bios.2015.09.025.

22. M. K. Masud, M. Umer, M. S. A. Hossain, Y. Yamauchi, N. Nguyen, and M. J. A. Shiddiky, "Nanoarchitecture Frameworks for Electrochemical MiRNA Detection," *Trends in Biochemical Sciences* 44, no. 5 (2019): 433–452, https://doi.org/10.1016/j.tibs.2018.11.012.

23. D. Wang, Y. Nie, Z. Li, and Q. Ma, "The Controllable Assembly of Cu Nanocluster-Based Aggregation Induced ECL Strategy for MiRNA Detection," *Analytica Chimica Acta* 1238 (1238): 340607, https://doi.org/10.1016/j.aca.2022.340607.

24. X. Wang, H. Liu, S. Zhang, et al., "Highly Sensitive ECL Detection of MiRNA Based on Self-Generated Coreactant and Target-Induced Catalyzed Hairpin Assembly," *Analytica Chimica Acta* 1324 (1324): 343103, https://doi.org/10.1016/j.aca.2024.343103.

25. T. Xu and Z. Geng, "Strategies to Improve Performances of LSPR Biosensing: Structure, Materials, and Interface Modification," *Biosensors and Bioelectronics* 174 (2021): 112850, https://doi.org/10.1016/j.bios.2020.112850.

26. M. Lin, C. Wang, R. Fan, et al., "Multi-Channel Prismatic Localized Surface Plasmon Resonance Biosensor for Real-Time Competitive Assay Multiple COVID-19 Characteristic MiRNAs," *Talanta* 275 (2024): 126142, https://doi.org/10.1016/j.talanta.2024.126142.

27. S. Park, J. Lee, and J. Yeo, "On-Chip Plasmonic Detection of MicroRNA-106a in Gastric Cancer Using Hybridized Gold Nanoparticles," *Sensors and Actuators B: Chemical* 262 (2018): 703–709, https://doi.org/10.1016/j.snb.2018.02.010.

28. L. Zhang, J. Wang, J. Zhang, et al., "Individual Au-Nanocube Based Plasmonic Nanoprobe for Cancer Relevant MicroRNA Biomarker Detection," *ACS Sensors* 2, no. 10 (2017): 1435–1440, https://doi.org/10.1021/acssensors.7b00322.

29. S. Song, J. U. Lee, M. J. Jeon, S. Kim, and S. J. Sim, "Detection of Multiplex Exosomal MiRNAs for Clinically Accurate Diagnosis of Alzheimer'S Disease Using Label-Free Plasmonic Biosensor Based on DNA-Assembled Advanced Plasmonic Architecture," *Biosensors and Bioelectronics* 199 (2022): 113864, https://doi.org/10.1016/j.bios.2021.113864.

30. J. J. Liu, H. H. Yan, Q. Zhang, et al., "High-Resolution Vertical Polarization Excited Dark-Field Microscopic Imaging of Anisotropic Gold Nanorods for the Sensitive Detection and Spatial Imaging of Intracellular MicroRNA-21," *Analytical Chemistry* 92, no. 19 (2020): 13118–13125, https://doi.org/10.1021/acs.analchem.0c02164.

31. H. H. Yan, M. Huang, F. Zhu, et al., "Two-Dimensional Analysis Method for Highly Sensitive Detection of Dual MicroRNAs in Breast Cancer Cells," *Analytical Chemistry* 95, no. 8 (2023): 3968–3975, https://doi.org/10.1021/acs.analchem.2c03479.

32. Y. Zhao, X. Gao, H. Wang, et al., "Ultrasensitive Detection of MicroRNA via a Au@Ag Nanosnowman," *Analytical Chemistry* 91, no. 24 (2019): 15988–15992, https://doi.org/10.1021/acs.analchem.9b04715.

33. A. Miti, S. Thamm, P. Müller, A. Csáki, W. Fritzsche, and G. Zuccheri, "A miRNA Biosensor Based on Localized Surface Plasmon Resonance Enhanced by Surface-Bound Hybridization Chain Reaction," *Biosensors and Bioelectronics* 167 (2020): 112465, https://doi.org/10.1016/j.bios.2020.112465.

34. M. Huang, R. Cheng, S. Wen, et al., "Ultrasensitive Detection of MicroRNA-21 in Human Serum Based on the Confinement Effect Enhanced Chemical Etching of Gold Nanorods," *Chinese Chemical Letters* 35, no. 9 (2024): 109379, https://doi.org/10.1016/j.cclet.2023.109379.

35. N. Zare, R. Ghasemi, L. Rafiee, and S. H. Javanmard, "Assessment of MicroRNA-21 Using Gold Nanoparticle-DNA Conjugates Based on Colorimetric and Fluorescent Detection," *Gold Bulletin* 55, no. 2 (2022): 107–114, https://doi.org/10.1007/s13404-022-00308-w.

36. Q. Wang, Q. Li, X. Yang, et al., "Graphene Oxide–Gold Nanoparticles Hybrids-Based Surface Plasmon Resonance for Sensitive Detection of MicroRNA," *Biosensors and Bioelectronics* 77 (2016): 1001–1007, https://doi.org/10.1016/j.bios.2015.10.091.

37. X. Miao, X. Ning, Z. Li, and Z. Cheng, "Sensitive Detection of MiRNA by Using Hybridization Chain Reaction Coupled With Positively Charged Gold Nanoparticles," *Scientific Reports* 6, no. 1 (2016): 32358, https://doi.org/10.1038/srep32358.

38. C. Li, Y. Zhang, Z. Ye, S. E. J. Bell, and Y. Xu, "Combining Surface-Accessible Ag and Au Colloidal Nanomaterials With SERS for in Situ Analysis of Molecule–Metal Interactions in Complex Solution Environments," *Nature Protocols* 18, no. 9 (2023): 2717–2744, https://doi.org/10.1038/s41596-023-00851-6.

39. H. Zhong, H. Ze, X. Zhang, et al., "In Situ SERS Probing the Effect of Additional Metals on Pt-Based Ternary Alloys Toward Improving ORR Performance," *ACS Catalysis* 13, no. 10 (2023): 6781–6786, https://doi.org/10.1021/acscatal.3c01317.

40. Y. Zhu, H. Tang, H. Wang, and Y. Li, "In Situ SERS Monitoring of the Plasmon-Driven Catalytic Reaction by Using Single Ag@Au Nanowires as Substrates," *Analytical Chemistry* 93, no. 34 (2021): 11736–11744, https://doi.org/10.1021/acs.analchem.1c01926.

41. L. Li, Y. Zhang, W. Zheng, X. Li, and Y. Zhao, "Optical Fiber SPR Biosensor Based on Gold Nanoparticle Amplification for DNA Hybridization Detection," *Talanta* 247 (2022): 123599, https://doi.org/10.1016/j.talanta.2022.123599.

42. P. Gong, Y. Wang, X. Zhou, et al., "In Situ Temperature-Compensated DNA Hybridization Detection Using a Dual-Channel Optical Fiber Sensor," *Analytical Chemistry* 93, no. 30 (2021): 10561–10567, https://doi.org/10.1021/acs.analchem.1c01660.

43. P. Zhang, X. Zhou, J. Jiang, et al., "In Situ Analysis of Membrane-Protein Binding Kinetics and Cell–Surface Adhesion Using Plasmonic Scattering Microscopy," *Angewandte Chemie International Edition* 61, no. 42 (2022): 61, https://doi.org/10.1002/anie.202209469.

44. H. Zhu, M. Lin, Y. Li, et al., "LSPR Sensing for in Situ Monitoring the Ag Dissolution of Au@Ag Core–Shell Nanoparticles in Biological Environments," *Spectrochimica Acta Part A: Molecular and Biomolecular Spectroscopy* 310 (2024): 123885, https://doi.org/10.1016/j.saa.2024.123885.

45. W. Zhang, G. Liu, J. Bi, K. Bao, and P. Wang, "Ultrasensitive Detection of Mercury (II) Ions (Hg^{2+}) Using the Localized Surface Plasmon Resonance (LSPR) Nanosensor and the Microfluidic Chip," *Sensors and Actuators a: Physical* 349 (2023): 114074, https://doi.org/10.1016/j.sna.2022.114074.

46. Z. Luo, Y. Wang, Y. Xu, et al., "Ultrasensitive U-Shaped Fiber Optic LSPR Cytosensing for Label-Free and in Situ Evaluation of Cell Surface N-Glycan Expression," *Sensors and Actuators B: Chemical* 284 (2019): 582–588, https://doi.org/10.1016/j.snb.2019.01.015.

Supporting Information

Additional supporting information can be found online in the Supporting Information section.

Supporting File: smll73845-sup-0001-SuppMat.docx.